Sensors and Materials, Vol. 21, No. 7 (2009) 403–418
MYU Tokyo

S & M 0780

Single-Charge Sensitivity of Single-Walled Carbon Nanotube Multifunctional Quantum Transistor

Takafumi Kamimura[1,2,3,*] and Kazuhiko Matsumoto[1,3,4]

[1]Advanced Industrial Science and Technology (AIST),
1-1-1 Umezono Tsukuba, Ibaraki 305-8568, Japan
[2]Japan Society for the Promotion of Science (JSPS),
6 Ichibancho, Chiyoda-ku, Tokyo 102-8471, Japan
[3]CREST, Japan Science and Technology Agency (JST), Kawaguchi Center Building 4-1-8,
Honcho, Kawaguchi-shi, Saitama 332-0012, Japan
[4]The Institute of Scientific and Industrial Research, Osaka University,
Mihogaoka 8-1, Ibaraki, Osaka 567-0047, Japan

(Received February 25, 2009; accepted May 12, 2009)

Key words: single-walled carbon nanotube, resonant tunneling transistor, single-hole transistor, single-charge sensitivity

Single-walled carbon nanotube (SWNT) field-effect transistors show hysteresis in their electrical characteristics owing to the amorphous carbon around the carbon nanotube. Here, we show the reduction in the hysteresis characteristic by a refining process applied repeatedly to the carbon nanotube. Moreover, an SWNT multifunctional quantum transistor that shows a transition between resonant transistor (RTT) characteristics and single-hole transistor (SHT) characteristics with a change in applied gate voltage is developed. By fabricating a few charge storage units around the channel of a purified SWNT multifunctional quantum transistor, an abrupt discrete switching of the source-drain current is observed, which corresponds to the single-charge transition between a storage unit and an SWNT. In addition, storage energy was controlled by adjusting applied bias.

1. Introduction

Various electrode materials for single-walled carbon nanotube (SWNT) transistors were investigated. Pd electrodes have been used for ohmic contacts,(1) Ti electrodes for Schottky contacts for hole conduction,(2–4) and Mg and Ca electrodes for electron conduction.(5) For sub-micron-order channel lengths at low temperatures, SWNT transistors with ohmic contacts have shown resonant tunneling transistor (RTT) characteristics,(6) which are also called Fabry-Perot characteristics, and SWNT transistors with Schottky contacts have shown single-hole transistor (SHT) characteristics,(7) in

*Corresponding author: e-mail: t.kamimura@aist.go.jp

which Schottky barriers act as tunneling barriers. Therefore, electrode materials should be carefully chosen to obtain the desired characteristics.

In this study, we succeeded in fabricating a multifunctional quantum transistor using the particle and wave natures of holes in an SWNT. This transistor can operate as an RTT and also as an SHT. An RTT is a device that uses the wave nature of holes and an SHT uses the particle nature of holes in the SWNT. Both devices need tunneling barriers on both sides of the quantum island. The RTT needs a strong coupling while the SHT needs a weak coupling between the quantum island and the electrodes. Usually, these tunneling barriers are fabricated from thin oxide layers. Therefore, the thickness of the tunneling barriers and coupling strength cannot normally be controlled in a given device. In the present device, however, the Schottky barriers act as tunneling barriers between the SWNT quantum island and the electrodes. Therefore, the thickness of the tunneling barriers and the coupling strength between the SWNT and the electrodes can be controlled by regulating the applied gate voltage V_G.

Moreover, an SWNT is a cylinder with a diameter of several nanometers. The small diameter makes it possible to detect an electrical field from even a single charge. Moreover, by observing the relative energy difference between the conducting carrier and the single charges to be measured, it is possible to define the potential energy of the single charges to be measured. However, as described in many reports,[8,9] SWNT electron devices show hysteresis characteristics in gate voltage-drain current characteristics. The hysteresis characteristics are caused by a gate-voltage-dependent charge fluctuation, *e.g.*, adsorption of water molecules around an SWNT,[8] charging into an insulator layer around an SWNT,[9] and charging into amorphous carbon around an SWNT.[3] By eliminating these origins of the hysteresis characteristics, the number of fluctuating charges decreases and a single charge can be detected by an SWNT multifunctional quantum transistor.

2. Materials and Methods

2.1 *Method*

We have eliminated the three main origins of the hysteresis characteristics of an SWNT field-effect transistor identified in recent reports.[3,8–10] To burn amorphous carbon, we annealed an SWNT at low temperature in an oxidizable atmosphere.[10] To reduce the number of adsorbed atmospheric molecules, we covered the channel with a silicon dioxide layer. To reduce the number of trap sites in the insulator, we reduced the channel length to 73 nm. The SWNT multifunctional quantum transistor fabricated by the process mentioned above shows almost no hysteresis characteristics in the gate voltage range from −40 to 40 V. Moreover, an abrupt discrete switching of the source-drain current is observed in the electrical measurements of the SWNT multifunctional quantum transistor at 7.3 K. These random telegraph signals (RTSs) are attributed to charge-fluctuating charge traps near the SWNT multifunctional quantum transistor conduction channel. The current-switching behavior associated with the occupation of individual electron traps is demonstrated and analyzed statistically.

2.2 *Sample preparations*

A schematic of the sample structure is shown in Fig. 1. The SWNT was prepared as follows. An n^+-Si wafer with a thermally grown 300-nm-thick oxide was used as a substrate. Layered Fe/Mo/Si (2 nm/20 nm/40 nm) catalysts were evaporated using an electron-beam evaporator under a vacuum of 10^{-6} Pa. These layered catalysts were patterned on the substrate using conventional photolithography. The SWNT was grown by thermal chemical vapor deposition (CVD) using mixed gases of hydrogen and argon-sparged ethanol. After the growth of the SWNT, it was purified by burning amorphous carbon around the SWNT in an air atmosphere at a temperature of several hundred degrees Celsius.(10) Ti (30 nm) electrodes were deposited on the patterned catalysts as the source and drain, and on the back surface of the n^+-Si substrate for the gate, using an electron-beam evaporator under a vacuum of 10^{-6} Pa. The distance (L) between the source and drain was 73 nm. Thus, a back-gate-type multifunctional quantum transistor with an SWNT channel that had the functions of an RTT and an SHT was fabricated. A single-charge measurement was carried out with a structure in which a silicon dioxide layer is on the SWNT channel.

3. Results and Discussions

Figure 2(a) shows the differential conductance dI_D/dV_D characteristic as a function of V_G at 7.3 K, where drain voltage was set at 8 mV. An oscillation characteristic with two oscillation periods is also observed in Fig. 2(a). A large oscillation period of ΔV_G = 1.1 V was observed at $V_G \geq -16$ V and a small oscillation period of ΔV_G = 0.65 V was observed at $V_G \leq -16$ V. Figure 2(b) shows the dI_D/dV_D peak on a linear scale at $V_G \geq -16$ V and $V_G \leq -16$ V. A clear difference in oscillation period is observed as follows. The peaks of dI_D/dV_D at $V_G \geq -16$ V are well fitted by a Gaussian, i.e., $G \approx \frac{2e^2}{h}\frac{T_L T_R}{\Gamma}\frac{1}{2kT}\exp\left(\frac{\varepsilon_F - \varepsilon_0}{2kT}\right)$, and at $V_G \leq -16$ V by a Lorentzian, i.e.,

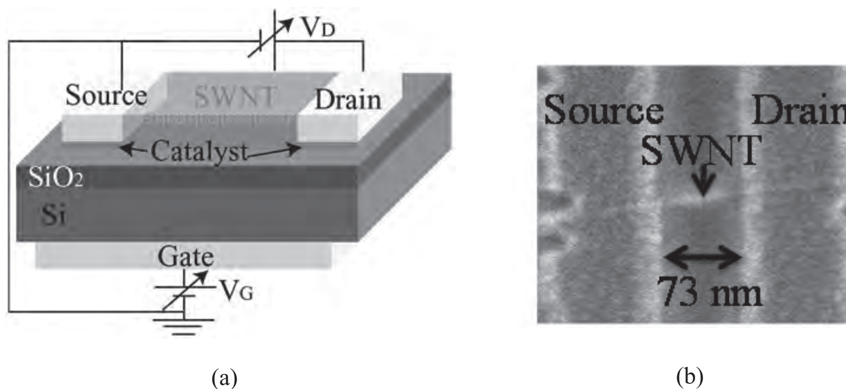

(a) (b)

Fig. 1. Schematic structure of SWNT multifunctional quantum transistor covered by silicon dioxide layer. The channel length is 73 nm. The inset shows a SEM image around the channel before silicon dioxide deposition. A few charge storages are fabricated in the SiO_2 layer.

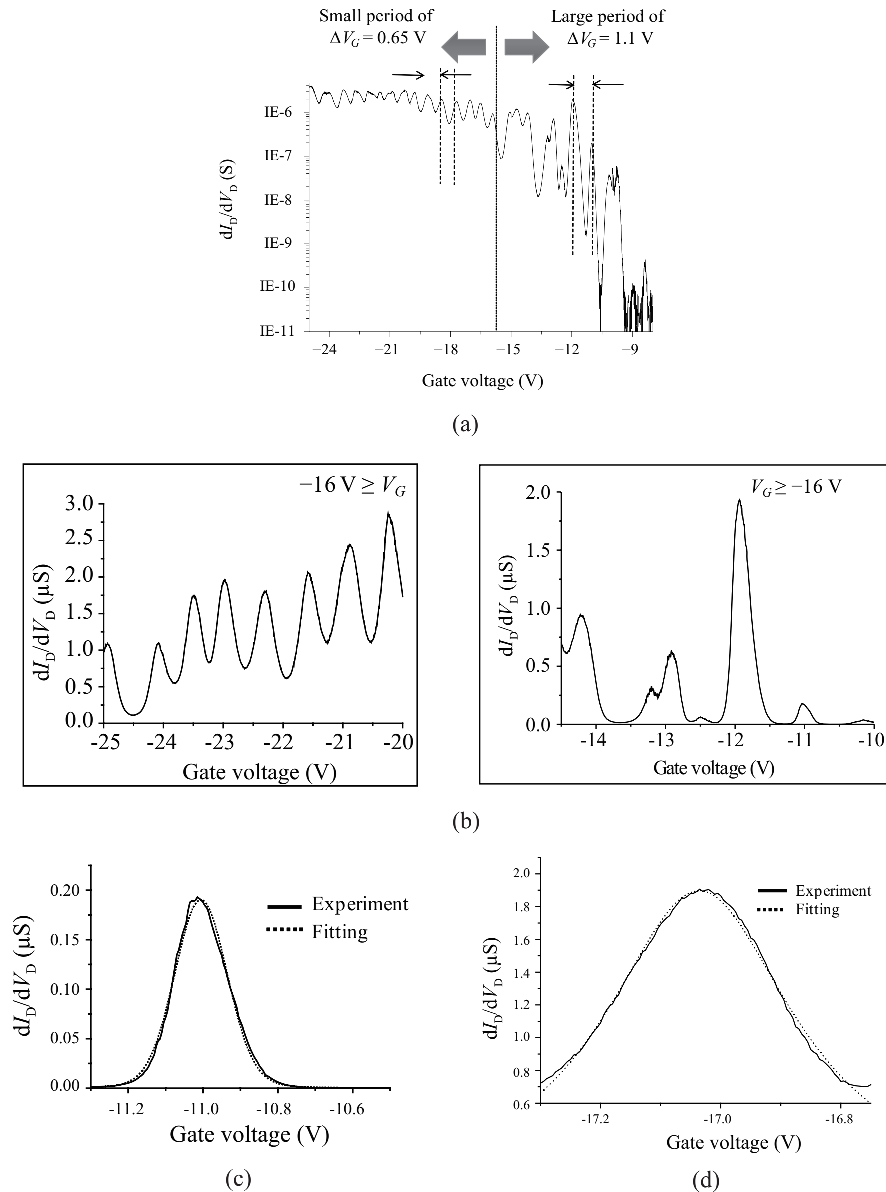

Fig. 2. (a) Differential conductance dI_D/dV_D characteristic as a function of V_G at 7.3 K. Two frequencies of oscillation were observed, which were ΔV_G = 1.1 and 0.65 V. (b) dI_D/dV_D peak in linear scale at low and high V_G values. (c) dI_D/dV_D peak at $V_G = -11$ V (black) and Gaussian fitting line (dotted). The peak is well fitted by the Gaussian function, which means that the shape of the peak can be attributed to thermal broadening. Therefore, the peak must be a Coulomb oscillation peak. (d) dI_D/dV_D peak at $V_G= -17$ V (black) and Lorentzian fitting line (dotted). The peak is well fitted by the Lorentzian function, which means that the shape of the peak can be attributed to energy uncertainty broadening. Therefore, the peak must be a resonant tunneling current peak.

$G = \frac{2e^2}{h} \frac{4T_L T_R}{(\varepsilon_F - \varepsilon_0)^2 + \Gamma^2}$, as shown in Figs. 2(c) and (d), respectively, where e is the elementary charge, h is Planck's constant, T_L and T_R are the tunneling probabilities at the left and right tunneling barriers, Γ is the full width at half maximum (FWHM), k is the Boltzmann constant, T is the temperature, ε_F is the Fermi level, and ε_0 is the quantum level. The shape of the Coulomb oscillation peaks must be Gaussian, which is attributed to thermal broadening, while the resonant tunneling current peaks must be Lorentzian, which is attributed to energy uncertainty.(9) Therefore, the dI_D/dV_D oscillations at $V_G \geq -16$ V in Fig. 2(a) should be Coulomb oscillation peaks, and those at $V_G \leq -16$ V in Fig. 2(a) should be resonant tunneling current peaks. In other words, the device operates in the particle nature mode at $V_G \geq -16$ V, and in the wave nature mode at $V_G \leq -16$ V.

Figure 3 shows the dI_D/dV_D characteristic as a function of drain voltage V_D at 7.3 K and $V_G = -12.795$ V. A dI_D/dV_D peak spacing of 26 mV is observed in the plot, which corresponds to the quantum energy level separation in the SWNT quantum island. The separation of the quantum energy levels is indicated by

$$\Delta E_Q = \left(\frac{hv_F}{2L}\right)\left[1 + \left(\frac{2L}{3rn}\right)^2\right]^{-\frac{1}{2}}, \quad (1)$$

where r is the radius of the SWNT, L is the length of the SWNT, and v_F is the Fermi velocity.(10) When n increases, the equation becomes

$$\Delta E_Q = \frac{hv_F}{2L}, \quad (2)$$

and shows a constant value independent of n. The energy separation ΔE_Q of the quantum levels for an SWNT length of 73 nm is calculated to be 24 mV from eq. (2). Because this estimated value of energy separation of 24 mV is in good agreement with the dI_D/dV_D

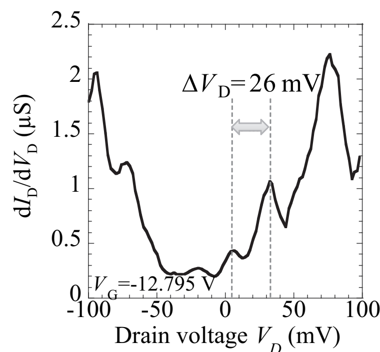

Fig. 3. dI_D/dV_D characteristic as a function of drain voltage V_D at $V_G = -12.795$ V and 7.3 K. The peaks are attributed to quantum energy levels in the SWNT. The estimated energy separation in 73 nm SWNT was 24 meV, which is in good agreement with the peak spacing of 26 mV in the plot.

peak spacing of 26 mV in Fig. 3, it can be concluded that the entire SWNT channel acts as a single quantum island.

Figure 4 shows a contour plot of the dI_D/dV_D characteristic as a function of V_G and V_D at 7.3 K. The characteristic can also be divided into two modes, the particle and wave

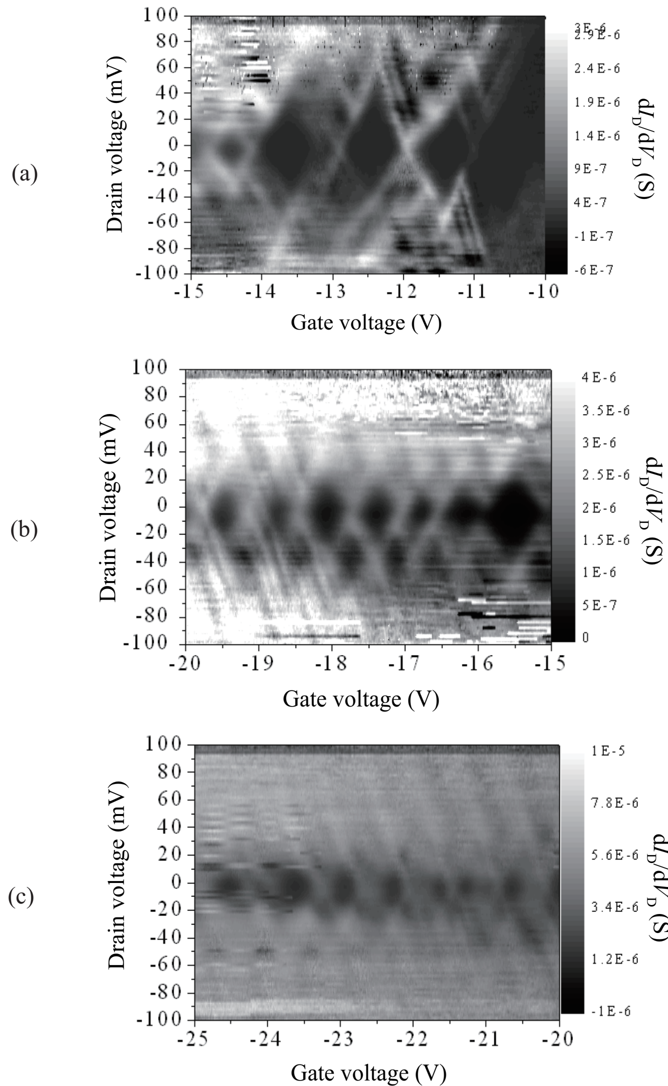

Fig. 4. Contour plot of dI_D/dV_D characteristic as a function of V_G and V_D at 7.3 K. (a) At $V_G \geq -16$ V, Coulomb diamond structures and line-shaped quantum levels outside of the Coulomb diamond structures are observed. Moreover, the Coulomb diamonds become smaller with increasingly negative V_G. (b) At $-16 \text{ V} \geq V_G \geq -20$ V, the Coulomb blockade is lifted and the Coulomb diamonds disappear. The quantum levels become blurry with increasingly negative V_G. The so-called Fabry-Perot quantum interference pattern is observed. (c) At $-20 \text{ V} \geq V_G$, the blurry quantum levels still remain.

nature modes. At $V_G \geq -16$ V, as shown in Figs. 4(a) and 4(b), the plot clearly shows the Coulomb diamond structures, which decrease in size with increasingly negative V_G. Additionally, line-shaped quantum levels are observed outside of these Coulomb diamond structures. Therefore, at $V_G \geq -16$ V, the device operated in the particle nature mode. As shown in Fig. 4(b), at $-16 \geq V_G \geq -20$ V, the Coulomb blockade was lifted and the Coulomb diamond structures disappeared at approximately $V_G = -16$ V. The quantum levels still remain and the so-called Fabry-Perot quantum interference pattern is observed in this region. Finally, at $V_G \leq -20$ V, the quantum levels become blurry with increasingly negative V_G, as shown in Fig. 4(c). Therefore, at -16 V $\geq V_G$, the device operated in the wave nature mode.

Figure 5(a) shows the Coulomb charging energy E_C as a function of V_G. E_C is obtained using $E_C = \Delta E - E_Q$, where ΔE is estimated from the size of the Coulomb diamonds. E_C markedly decreases with negatively increasing V_G, almost reaching zero at $V_G \geq -16$ V. Therefore, the Coulomb diamonds disappear at -16 V $\geq V_G$. The tunneling capacitance C_t and the gate capacitance C_G as a function of V_G are shown in Fig. 5(b). C_t and C_G are obtained from $C_t = e/2E_C - C_G$ and $C_G = e/\Delta V_G$, respectively. C_t depends on the thickness of the tunneling barrier and C_G depends on the gate structure. C_t drastically increases with negatively increasing V_G, while C_G is almost constant, independent of V_G. The marked increase in C_t is attributed to the decrease in the thickness of the Schottky barriers at the contacts between the SWNT quantum island and the electrodes.[1] When the Schottky barriers become thin with negatively increasing V_G, as shown in the inset of Fig. 5(b), C_t markedly increases and the coupling strength of the wave function between the outside and inside of the Schottky barrier increases. Therefore, the Coulomb blockade is lifted and E_C becomes zero at -16 V$\geq V_G$.

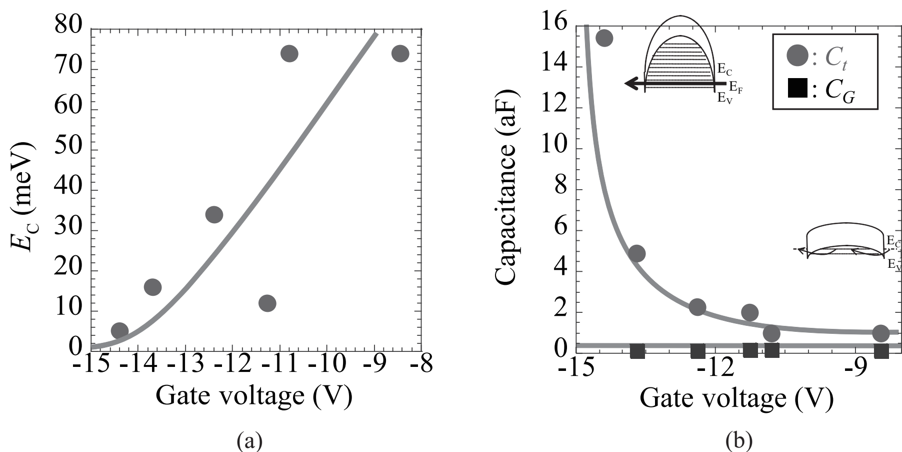

Fig. 5. (a) Coulomb charging energy E_C as a function of V_G. E_C markedly decreases at $V_G \geq -16$ V and reaches zero at approximately $V_G = -16$ V. Therefore, the Coulomb diamonds disappear in the mid-V_G region. (b) Tunneling capacitance C_t and gate capacitance C_G characteristics as functions of V_G. C_t markedly increases at $V_G \geq -16$ V. On the other hand, C_G is almost constant, independent of V_G. The marked increase in C_t is attributed to the change in the thickness of the Schottky barriers at the contact between the SWNT channel and the electrodes.

The dependence of the FWHM of the resonant tunneling current peak characteristic on V_G is shown in Fig. 6(a). The FWHM is estimated from an I_D-V_G plot using the Voigt function, which is a convolution of the Gaussian and Lorentzian functions, and

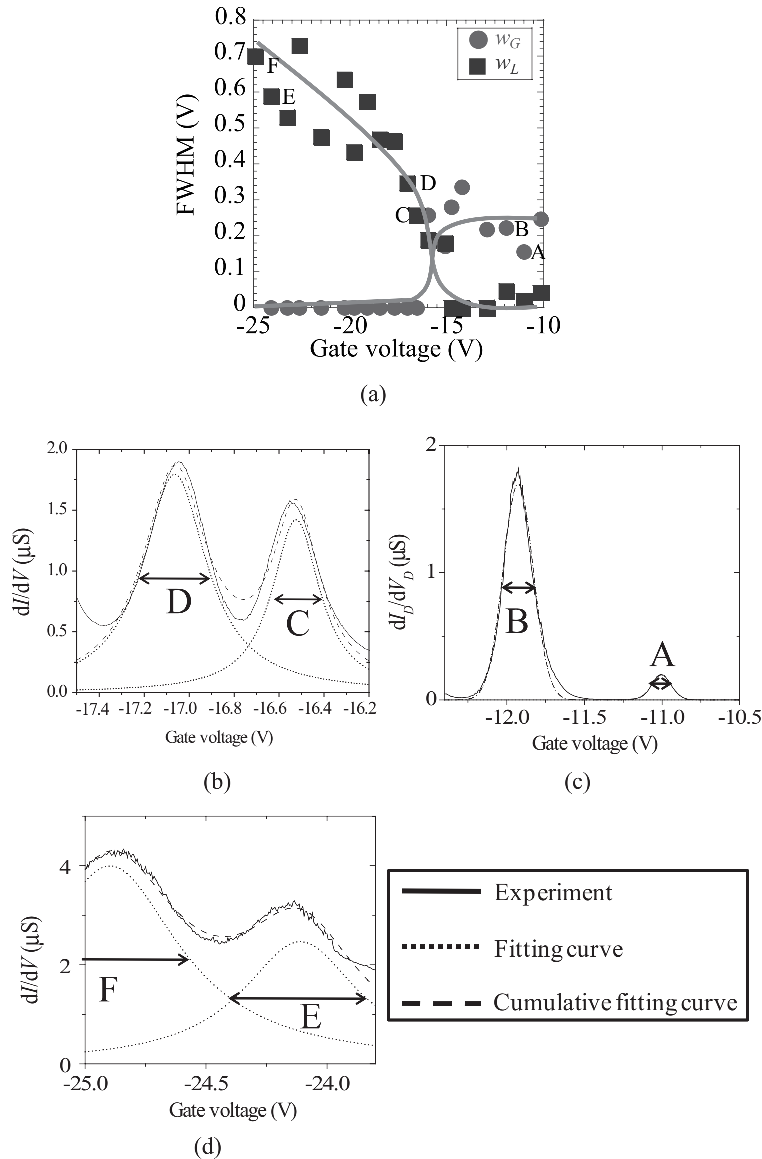

Fig. 6. (a) FWHM of the dI_D/dV_D peak characteristics as a function of V_G. w_G is almost constant independent of V_G, and w_L is negligible at $V_G \geq -16$ V. w_G becomes vanishingly small and w_L increases linearly with increasingly negative V_G at $-16 \text{ V} \geq V_G$. (b)–(d) FWHMs: the experimental data are indicated by the solid lines, the fitting curves are indicated by the dotted lines, the cumulative fitting curves are indicated by the dashed lines, and each alphabetic marker for a peak corresponds to a marker in the plot in Fig. 6(a).

can be used to divide the FWHM into the FWHM of the Gaussian w_G and that of the Lorentzian w_L. Figures 6(b)–6(d) show several curves fitted by the Voigt function, where the black lines are the experimental data, the dotted lines are the fitting curves, the dashed lines are the cumulative fitting curves, and each alphabetic marker for peaks A-F corresponds to a marker in the plot of Fig. 6(a). In the particle nature mode of $V_G \geq -16$ V, w_L is negligible and the w_G of about 0.2 V is independent of V_G because the FWHM of the Coulomb oscillation mainly depends on the thermal broadening of Fermi dispersion.[11] On the other hand, in the wave nature mode of $-16 \text{ V} \geq V_G$, w_G becomes negligible and w_L increases linearly with increasingly negative V_G. w_L is proportional to tunneling probability as follows: $\alpha w_L = T\hbar v_F/2L$, where α is the ratio of modulated energy to applied V_G, and T is the tunneling probability.[12] Therefore, the increase in w_L seen in Fig. 6 represents an increase in tunneling probability, which is attributed to a decrease in the thickness of the Schottky barriers with increasingly negative V_G.

The logarithmic dependence of the drain current I_D on the inverse of the temperature is shown in Fig. 7. At $V_G = -38$ V of the wave nature mode, I_D is almost constant, which is independent of temperature. In the wave nature mode, the Schottky barrier is so thin that tunneling current becomes predominant. In contrast, at $V_G = -10$ V of the particle nature mode, I_D drastically increases in the high-temperature region, and the Schottky barrier height $\Delta\Phi$, as estimated from the slope, is $\Delta\Phi = 50$ mV. In the particle nature mode, the Schottky barriers are so thick that the thermal emission current becomes predominant in the high-temperature region. These results indicate that the tunneling probabilities at the Schottky barriers can be modulated by controlling the applied V_G and that the coupling between the SWNT quantum island and the electrodes is strong in the wave nature mode, but weak in the particle nature mode.

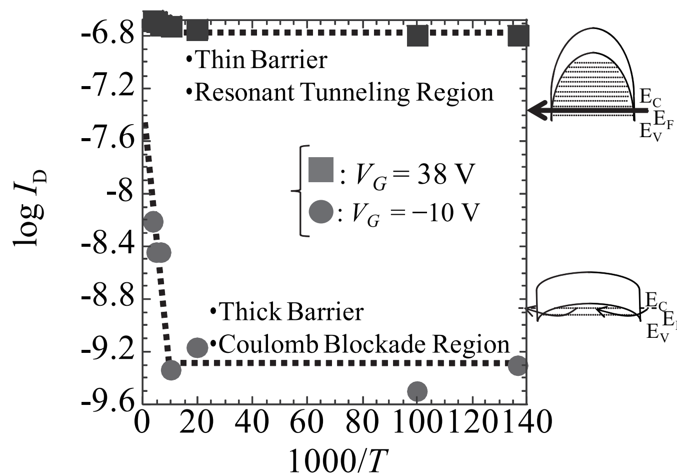

Fig. 7. Logarithmic dependence of the drain current I_D on the inverse of the temperature. At $V_G = -38$ V of the wave nature mode, I_D is almost constant independent of temperature. In the wave nature mode, the Schottky barrier is so thin that tunneling current becomes predominant. In contrast, at $V_G = -10$ V in the particle nature mode, I_D markedly increases in the high-temperature region, and the Schottky barrier height estimated from the slope is $\Delta\Phi = 50$ mV.

Figure 8 shows the temperature dependence of differential conductance as a function of gate voltage. The quantum level peaks became blurry with increasing temperature. However, even at $T = 100$ K, the quantum levels still remained, as indicated by arrows.

The static characteristic measurement of the device with a silicon dioxide layer on the SWNT channel shown in Fig. 9 was carried out using Agilent B 1500. In the measurement, the data were integrated for a few seconds to eliminate the effect of noise, which was set using the equipment automatically. After that, the data were recorded. From the drain current I_D-gate voltage V_G characteristics of the SWNT multifunctional quantum transistor at a drain voltage of 11 mV at 7.3 K, the drain current showed a periodic peak-and-valley structure with two periods. As shown in Fig. 9(a), I_D was observed only in the negative-V_G region, which indicates that the measured SWNT was a p-type semiconductor. Moreover, a large period of ~3 V at approximately $V_G = 0$ V was observed, which was attributed to the Coulomb oscillation characteristic. Part of Fig. 9(a) is expanded in the horizontal scale and is shown in Fig. 9(b), where a small period of $\Delta V_G = 0.65$ V was observed at a higher V_G, which was attributed to the Fabry-Perot interference property[6] of holes, the coherent length of which was more than 73 nm, and coherent transport in the entire channel was achieved. Figure 9(c) shows a contour plot of the second-order differential conductance as a function of gate and drain voltages, in which a clear Fabry-Perot interference pattern can be seen.

From a small period of drain current oscillation of $\Delta V_G = 0.65$ V and the equation[12] $\Delta E_Q = \alpha V_G = \mathrm{h}v_F/2Le$, where ΔE_Q is the quantum energy separation, α is the gate modulation coefficient, h is Planck's constant, v_F is the Fermi velocity in graphene, L is the length of the cavity of the hole, and e is the elementary charge, we estimated the width of the quantum well and obtained the length of the cavity of the hole L to be 55

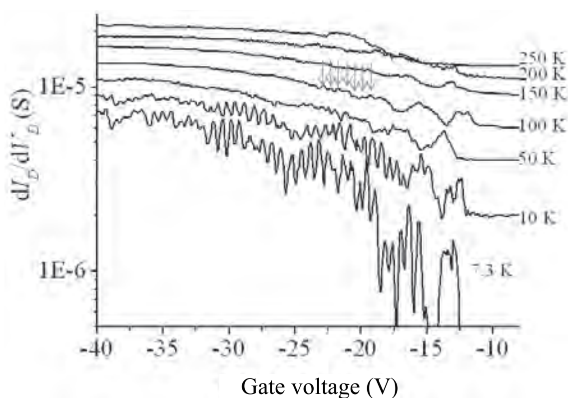

Fig. 8. Temperature dependence of differential conductance on V_G. Each plot is shifted by 3 μS for easier visualization. The quantum level peaks become blurry with increasing temperature. However, even at $T = 100$ K, the quantum levels remain, as indicated by the arrows.

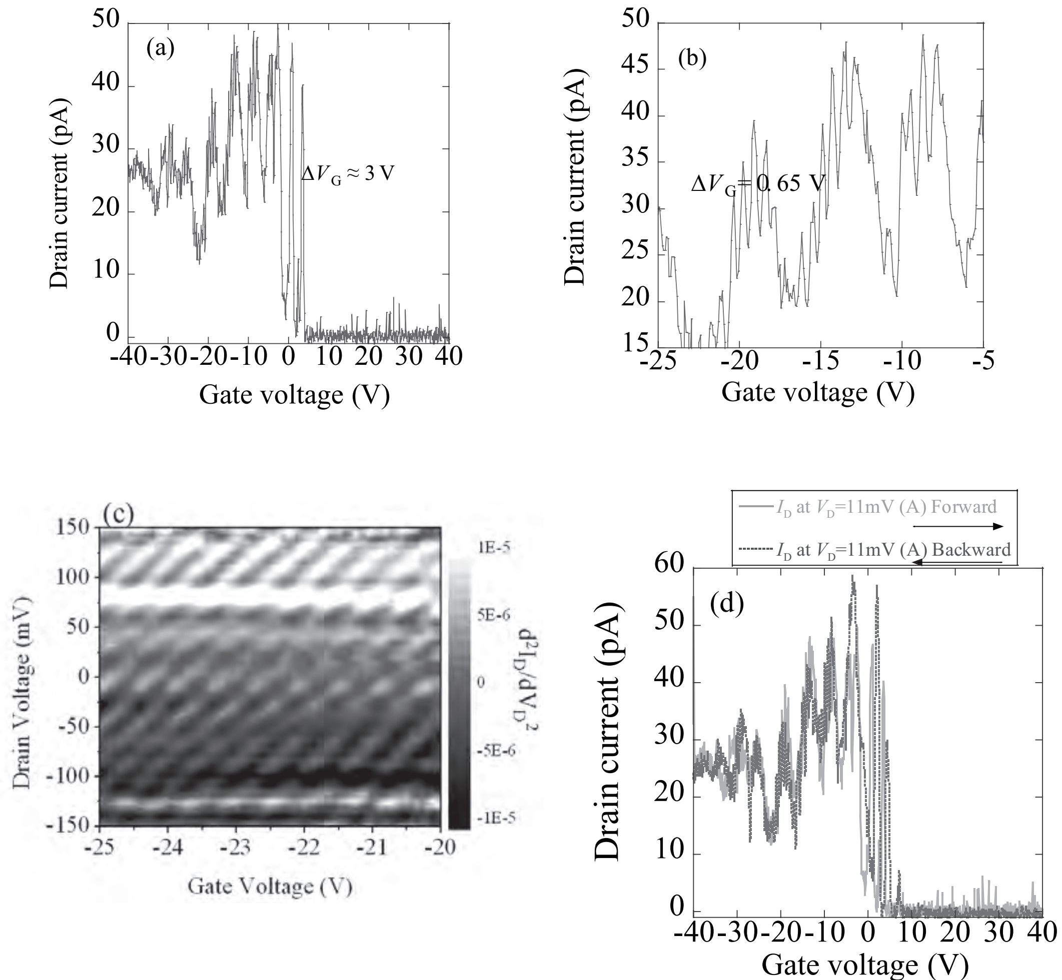

Fig. 9. (a) Coulomb oscillation characteristic at 7.3 K. Drain current was observed only in negative-gate-voltage regions, which indicates that the measured SWNT is a p-type semiconductor. A large period of ~3 V at an applied gate voltage of about V_G = 0 V was observed, which was attributed to a Coulomb oscillation characteristic. (b) The small period of ΔV_G = 0.65 V of drain current peaks at 7.3 K, which was attributed to the quantum interference property, namely, Fabry-Perot interference of a hole, the coherent length of which was more than 73 nm. Coherent transport in the entire channel was achieved. (c) Contour plot of second-order differential conductance as a function of gate and drain voltages at 7.3 K, which shows a clear Fabry-Perot interference pattern. (d) Drain current-gate voltage characteristics with round-trip applied gate voltage being swept from V_G = 40 to −40 V after being swept from V_G = −40 to 40 V at 7.3 K. The two drain current characteristics almost overlapped.

nm. The estimated value is in agreement with the channel length of 73 nm of the device, which was obtained by scanning electron microscopy (SEM) (inset of Fig. 1). The slight difference between the estimated L and the channel length must be attributed to the width of band bending in the SWNT, *e.g.*, Schottky barriers.

In Fig. 9(d), the gray (black) line shows drain current vs applied gate voltage from −40 (40) to 40 (−40) V in a forward (backward) sweep of gate voltage. The SWNT multifunctional quantum transistor showed almost no hysteresis characteristics. The SWNT multifunctional quantum transistor was covered with a silicon dioxide layer, which prevents the SWNT from absorbing and releasing molecules in ambient, because the fluctuation of molecules on the SWNT usually induces the hysteresis characteristics in the drain current-gate voltage characteristics. Moreover, the SWNT multifunctional quantum transistor has a small channel length of 73 nm, which reduces the number of trap sites near the SWNT as well as the number of trapped carriers causing hysteresis characteristics. We believe that the purification is effective for reducing the hysteresis characteristics. Thus, the hysteresis characteristic in the drain current-gate voltage characteristic was eliminated.

Figure 10(a) shows the time dependence of the conductance of the SWNT multifunctional quantum transistor at 7.3 K with a gate bias of $V_G = -25.36$ V. A short sampling time of 10 ms was set in the dynamic characteristic measurements shown in Fig. 10. The applied gate voltage was in the Fabry-Perot interference region. The SWNT multifunctional quantum transistor shows RTS, as shown in Fig. 10(a). The RTS showed three levels, n, n+1, and n+2, of the conductance shown in Fig. 10(a). At a lower applied gate voltage, current levels higher than n+2 such as n+3 and n+4 appeared. The multiple levels of RTS are attributed to charge-fluctuating charge storage units near the conduction channels of the SWNT multifunctional quantum transistor. Moreover, because there was a single-charge storage unit including multiple energy levels or there were some charge storage units located at almost the same distances from the conductance channel of the SWNT multifunctional quantum transistor, the RTS appeared.

Figures 10(b) and 10(c) show histograms of the conductance levels of RTS at V_G = −25.36 and −25.39 V, respectively. The three peaks of the conductance levels of RTS expressed as P_n, P_{n+1}, and P_{n+2} are shown in Figs. 10(b) and 10(c). The conductance levels of the three peaks directly correspond to the conductance levels of RTS. On the other hand, the relative heights of the peaks correspond to occupation probabilities at each conductance level of the RTS. The heights of the peaks depend on applied gate voltage. P_n decreases and P_{n+1} and P_{n+2} increase with slightly increasing applied gate voltage from $V_G = -25.36$ to −25.39 V, which means that the energy levels in the charge storage unit are modulated by applied gate voltage.

The gate voltage dependences of the natural log of the ratio between the m_{th} peak and the $(m+1)_{th}$ peak in the conductance histogram P_{m+1}/P_m ($m = n, n+1, n+2, \cdots, n+4$) are shown in Fig. 11(a). Figures 11(b)–11(e) are enlarged plots of each P_{m+1}/P_m ($m = n, n+1, n+2, \cdots, n+4$). The natural log of P_{m+1}/P_m linearly depends on applied gate voltage and saturates at each V_G. Each starting point of saturation is marked by an arrow in Fig. 11(a). The charge storage energy levels are floating. Therefore, the modulations of energy by V_G may differ at each charge storage unit. We think that the natural log of

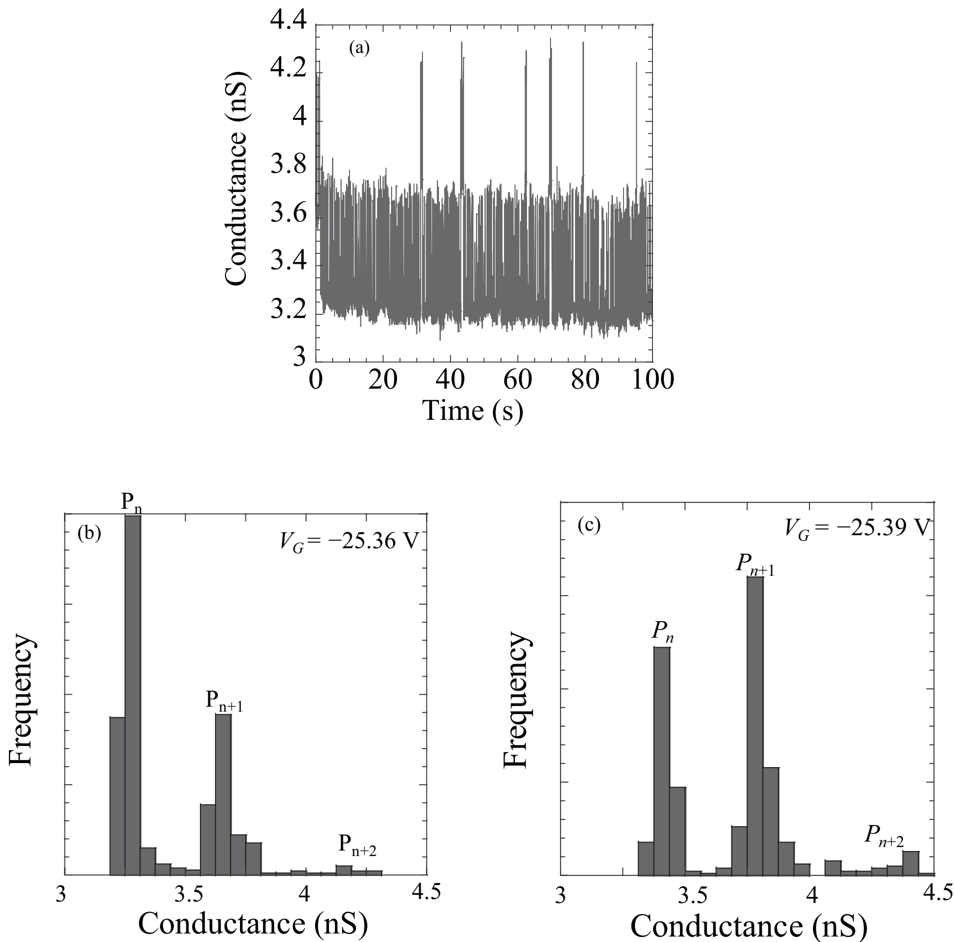

Fig. 10. (a) Time dependence of drain current with RTS at a gate voltage of $V_G = -25.36$ V. The time dependence of drain current was sampled for 100 s and the sampling time was 10 ms; (b) and (c) show histograms of the conductance levels of RTS at $V_G = -25.36$ and -25.39 V, respectively. P_n decreases and P_{n+1} and P_{n+2} increase with slightly increasing applied gate voltage from $V_G = -25.36$ to -25.39 V.

P_{m+1}/P_m saturates at each V_G owing to the difference in energy modulation by V_G at each charge storage unit.

The charge transition is modeled, as shown in Fig. 12(a), in which the energy barrier is between the SWNT and the charge storage unit. The energy difference ΔE_n between the charge storage energy level E_n and the Fermi level E_f is expressed as $\Delta E_n = E_f - E_n$, which is modulated by the applied gate voltage V_G. According to equilibrium statistical mechanics, P_{m+1}/P_m is given by[13]

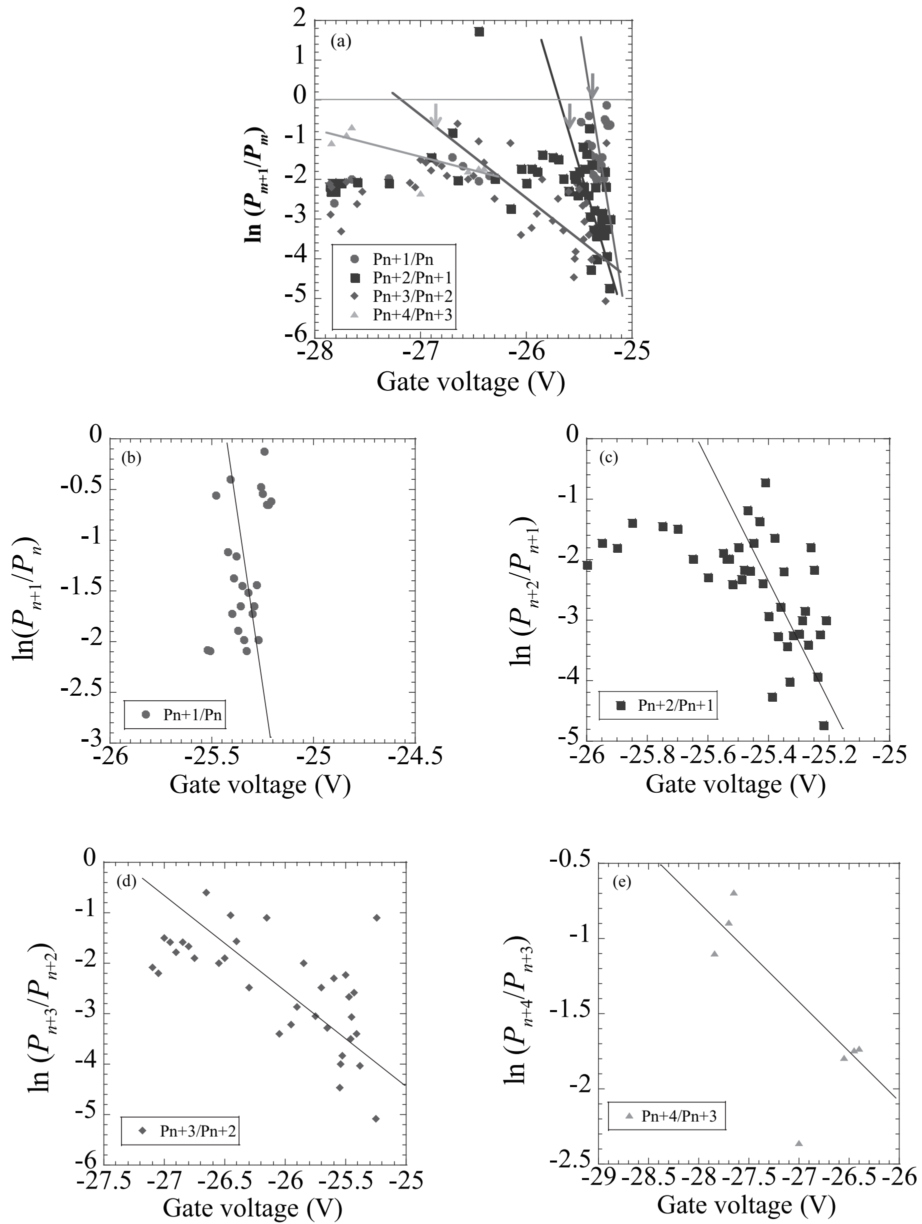

Fig. 11. (a) Gate voltage dependence of the natural log of the ratio between the occupancy probabilities of the m_{th} current levels P_{n+1}/P_n. (b)–(e) Enlarged plots of each P_{m+1}/P_m ($m = n$, n+1, n+2,···n+4). The natural log of $P_{n+}1/P_n$ was linearly dependent on gate voltage, the slopes of which are −10.4, −4.78, −1.47, and −0.690 V^{-1}, respectively.

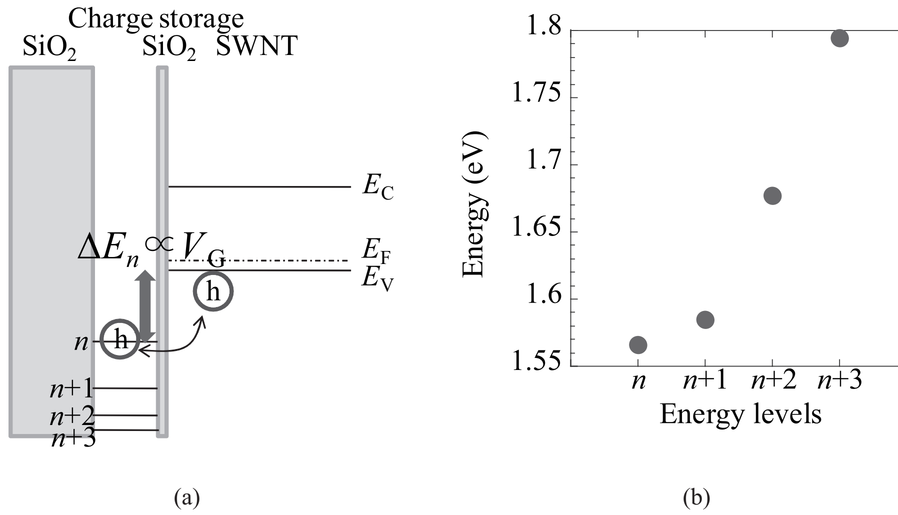

(a) (b)

Fig. 12. (a) Schematic model of charge storage. When the charge storage energy level is coincident with the top of the valence band owing to applied gate voltage, the carrier departs and arrives between them through the barrier with tunneling. The exiting probabilities of the carrier at the charge storage and valence band depend on the relative height of their energy levels under equilibrium condition. (b) Estimated charge storage energy levels from the dependence of P_{n+1}/P_n on V_G shown in Figs. 11(b)–11(e) and eq. (3). The energy levels increase from 0.17 to 0.28 eV with increasing number of energy levels in the region of V_G from −25 to −28 V.

$$P_{m+1}/P_m = (g_f/g_S)\, e^{-\beta(E_f - E_n)} = (g_f/g_S)e^{-\beta\Delta E_n}, \tag{3}$$

where g_f and g_S are the degeneracies of the top of the valence band and the charge storage unit, respectively. g_f/g_S is assumed to be 1. β is 1/kT. E_n includes the contributions of the *e* electrostatic potential induced by V_G, the intrinsic energy level in the storage unit, and the Coulomb charging energy. The basis of eq. (3) is the Arrhenius equation. In this model, the height of the barrier is the energy difference between E_f and E_n. Assuming a linear dependence of ΔE_n on V_G, ΔE_n can be written as $\Delta E_n = \alpha e(V_0 - V_G)$, where α is the gate modulation coefficient that has a constant value of 0.062. α is obtained from the periods of Fabry-Perot interference characteristic on V_D and V_G. V_0 is the offset voltage obtained from the intersecting points of the extrapolating line of the fitting lines and the line of $\ln(P_{m+1}/P_m) = 0$. Therefore, eq. (3) is transformed to

$$\ln(P_{m+1}/P_m) = -\beta e\alpha(V_0 - V_G). \tag{4}$$

Equation (4) is the transformed Arrhenius equation, in which V_G is the parameter.

From the dependence of P_{n+1}/P_n on V_G shown in Fig. 11 and eqs. (3) and (4), ΔE_n can be obtained and is shown in Fig. 12(b). The obtained energy levels are from 1.57 to 1.79 eV.

4. Summary

In summary, we succeeded in fabricating and demonstrating a multifunctional quantum transistor using the particle and wave natures of holes in SWNT. This transistor can operate in the wave nature mode as an RTT and in the particle nature mode as an SHT. We were able to reveal that the principle of the characteristic transition from an SHT to an RTT is the modulation of the coupling strength between the SWNT quantum island and the electrodes by the applied V_G.

The fabrication of the charge storage unit, the detection of single-charge transitions near the channel of the SWNT multifunctional quantum transistor at 7.3 K, and the estimation of the energy differences between the energy levels of the SWNT multifunctional quantum transistor and the storage carriers have been demonstrated. The observed RTS was dependent on applied V_G. We were able to estimate the energy levels in the charge storage unit from the gate voltage dependence of RTS.

References

1 A. Javey, J. Guo, Q. Wang, M. Lundstrom and H. Dai: Nature **424** (2003) 654.
2 S. Heinze, J. Tersoff, R. Martel, V. Derycke, J. Appenzeller and Ph. Avouris: Phys. Rev. Lett. **89** (2002) 106801-1.
3 R. Martel, V. Derycke, C. Lavoie, J. Appenzeller, K. K. Chan, J. Tersoff and Ph. Avouris: Phys. Rev. Lett. **87** (2001) 256805-1.
4 T. Kamimura and K. Matsumoto: Jpn. J. Appl. Phys. **44** (2005)1603.
5 Y. Nosho, Y. Ohno, S. Kishimoto and T. Mizutani: Nanotechnology **17** (2006) 3412.
6 W. Liang, M. Bockrath, D. Bozovic, J. H. Hafner, M. Tinkham and H. Park: Nature **411** (2001) 665.
7 M. Suzuki, K. Ishibashi, T. Ida, D. Tsuya, K. Toratani and Y. Aoyagi: J. Vac. Sci. Technol. B **19** (2001) 2770.
8 W. Kim, A. Javey, O. Vermesh, Q. Wang, Y. Li, and H. Dai: Nano Lett. **3** (2003) 193.
9 M. Radosavljevic´, M. Freitag, K. V. Thadani, and A. T. Johnson: Nano Lett. **2** (2002) 761.
10 T. Kamimura and K. Matsumoto: IEICE Trans. Electron. **E87-C** (2004) 1795.
11 E. B. Foxman, P. L. McEuen, U. Meirav, N. S. Wingreen, Y. Meir, P. A. Belk and S. J. Wind: Phys. Rev. B **47** (1993) 10020.
12 T. Kamimura and K. Matsumoto: Jpn. J. Appl. Phys. **45** (2006) 338.
13 H. B. Peng, M. E. Hughes and J. A. Golovchenkoa: Appl. Phys. Lett. **89** (2006) 243502.